

DETC2009-87537

DIRECT SIMULATION BASED MODEL-PREDICTIVE CONTROL OF FLOW MALDISTRIBUTION IN PARALLEL MICROCHANNELS

Mathieu Martin, Chris Patton, John Schmitt and Sourabh V. Apte*

School of Mechanical, Industrial and Manufacturing Engineering
Oregon State University
Corvallis, OR 97331

ABSTRACT

The goal of this investigation is to develop a simulation-based control strategy to eliminate flow-maldistribution in parallel microchannels. An accurate simulation of fluid flow through parallel microchannels is achieved by utilizing a fictitious domain representation of immersed objects, such as microvalves and bubbles. System identification techniques are employed to produce a lower dimensional model that captures the essential dynamics of the full nonlinear flow, in terms of a relationship between the valve angles and the exit flow rate for each channel. The resulting linear model is incorporated into a model predictive control scheme to identify flow maldistribution from exit flow velocities and prescribe actuation of channel valves to effectively redistribute the flow. Flow simulations in a three parallel microchannel geometry including bubbles illustrates the effectiveness of the control design, which quickly and efficiently varies channel valves to remove the bubble and equalize the flow rates in each channel.

INTRODUCTION

Modern tactical energy systems, such as soldier portable power and cooling systems, utilize microchannels in heat sinks and heat exchangers to efficiently transfer heat from one source to another. For improved efficiency and cooling of high heat loads, two-phase flows involving convective boiling of high latent heat fluids are used. Two-phase flows with vapor bubbles

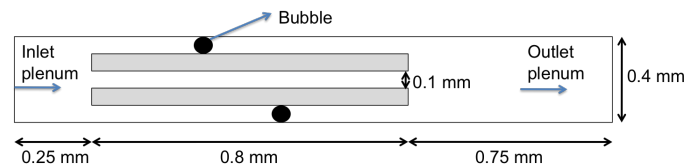


Figure 1: Schematic of parallel microchannels with bubbly flow.

also exist in condensers and evaporators. Formation and growth of these vapor bubbles inside microchannels can lead to blocking effects resulting in flow maldistribution together with non-uniform spatial and temporal conditions. This may lead to increased pressure-drops, local burn-outs and a drastic decrease in performance of the systems under consideration.

This work presents a numerical simulation of flow maldistribution in a parallel-microchannel geometry. We consider the bubbly flow regime with one or more bubbles present in a parallel microchannel configuration as shown in Fig. 1. In order to restore a nominal flow through the geometry, valves have been added. Utilizing mass flow rate information, the controller actuates the valves to restore the nominal regime of the device.

FLOW SOLVER

The computations carried out in this work utilize direct numerical simulation (DNS) with fictitious domain representation of arbitrary shaped immersed objects such as the microvalves and bubbles. The fictitious domain approach (Glowinski et al. [1],

*Corresponding Author: e-mail: sva@enr.orst.edu, phone: 541-737-7335, fax: 541-737-2600

Patankar [2], Apte et al. [3]) allows accurate representation of moving boundaries embedded in a fluid flow. Two types of moving boundaries are considered in this study: (i) specified motion of the immersed object and (ii) freely moving objects. The motion of the microvalves is a *specified* rigid body motion consisting of translation and rotational velocities. The bubbles or particles are allowed to move *freely*. Their motion is obtained by directly computing the forces acting on them. As the first step, we assume the bubbles as *rigid* objects immersed in a surrounding viscous fluid. As shown later, such an assumption is reasonable for low Reynolds numbers and high Weber numbers. For small Weber numbers, the inertial shearing forces acting on the bubble are much smaller than the surface tension forces. Under these conditions bubble deformation is minimal, the shape of the bubble is preserved. One consequence of this assumption is that modeling the motion of the bubble is much easier; the region occupied by the bubble is forced to undergo rigid body motion consisting of only translation and rotation. The bubble motion is then obtained directly by using a novel algorithm based on fictitious domain method for high-density ratios between the fluid and the immersed object. In this fully resolved simulation approach, models for drag, lift, or added mass forces on the bubble are not required, but such forces are directly computed. Below we describe in detail the computational approach for freely moving rigid objects immersed in a viscous, incompressible fluid. Details of the numerical scheme and several verification and validation test cases are also presented to show good predictive capability of the numerical solver.

Let Γ be the computational domain which includes both the fluid ($\Gamma_F(t)$) and the particle ($\Gamma_P(t)$) domains. Let the fluid boundary not shared with the particle be denoted by \mathcal{B} and have a Dirichlet condition (generalization of boundary conditions is possible). For simplicity, let there be a single rigid object in the domain and the body force be assumed constant so that there is no net torque acting on the object. The basis of fictitious-domain based approach [1] is to extend the Navier-Stokes equations for fluid motion over the entire domain Γ inclusive of immersed object. The natural choice is to assume that the immersed object region is filled with a Newtonian *fluid* of density equal to the object density (ρ_P) and some fluid viscosity (μ_F). Both the real and fictitious fluid regions will be assumed as incompressible and thus incompressibility constraint applies over the entire region. In addition, as the immersed objects are assumed rigid, the motion of the material inside the object is constrained to be a rigid body motion. Several ways of obtaining the rigidity constraint have been proposed ([1, 2, 4]). We follow the formulation developed by Patankar [4] and described in detail by Apte et al. [3]. A brief description is given here for completeness.

The momentum equation for fluid motion applicable in the

entire domain Γ is given by:

$$\rho \left(\frac{\partial \mathbf{u}}{\partial t} + (\mathbf{u} \cdot \nabla) \mathbf{u} \right) = -\nabla p + \nabla \cdot \left(\mu_F \left(\nabla \mathbf{u} + (\nabla \mathbf{u})^T \right) \right) + \rho \mathbf{g} + \mathbf{f}, \quad (1)$$

where ρ is the density field, \mathbf{u} the velocity vector, p the pressure, μ_F the fluid viscosity, \mathbf{g} the gravitational acceleration, and \mathbf{f} is an additional body force that enforces rigid body motion within the immersed object region Γ_P . The fluid velocity field is constrained by the conservation of mass which for an incompressible fluid simply becomes: $\nabla \cdot \mathbf{u} = 0$.

In order to enforce that the material inside the immersed object moves in a rigid fashion, a rigidity constraint is required that leads to a non-zero forcing function \mathbf{f} . Inside the particle region, the rigid body motion implies vanishing deformation rate tensor:

$$\left. \begin{aligned} \frac{1}{2} \left(\nabla \mathbf{u} + (\nabla \mathbf{u})^T \right) &= \mathbf{D}[\mathbf{u}] = 0, \\ \Rightarrow \mathbf{u} &= \mathbf{u}^{RBM} = \mathbf{U} + \Omega \times \mathbf{r} \end{aligned} \right\} \text{in } \Gamma_P, \quad (2)$$

where \mathbf{U} and Ω are the translation and angular velocities of the object and \mathbf{r} is the position vector of a point inside the object from its centroid.

The vanishing deformation rate tensor for rigidity constraint automatically ensures the incompressibility constraint inside the particle region. The incompressibility constraint gives rise to the scalar field (the pressure, p) in a fluid. Similarly, the tensor constraint $\mathbf{D}[\mathbf{u}] = 0$ for rigid motion gives rise to a tensor field inside the particle region. A fractional-step algorithm can be devised to solve the moving boundary problem [3,4]. Knowing the solution at time level t^n the goal is to find \mathbf{u} at time t^{n+1} .

1. In this first step, the rigidity constraint force \mathbf{f} in equation 1 is set to zero and the equation together with the incompressibility constraint (equation 2) is solved by standard fractional-step schemes over the entire domain. Accordingly, a pressure Poisson equation is derived and used to project the velocity field onto an incompressible solution. The obtained velocity field is denoted as \mathbf{u}^{n+1} inside the fluid domain and $\hat{\mathbf{u}}$ inside the object.
2. The velocity field for a freely moving object is obtained in a second step by projecting the flow field onto a rigid body motion. Inside the object:

$$\rho_P \left(\frac{\mathbf{u}^{n+1} - \hat{\mathbf{u}}}{\Delta t} \right) = \mathbf{f}. \quad (3)$$

To solve for \mathbf{u}^{n+1} inside the particle region we require \mathbf{f} . The constraint on the deformation rate tensor given by equation 2

can be reformulated to obtain:

$$\nabla \cdot (\mathbf{D}[\mathbf{u}^{n+1}]) = \nabla \cdot \left(\mathbf{D} \left[\hat{\mathbf{u}} + \frac{\mathbf{f}\Delta t}{\rho} \right] \right) = 0; \quad (4)$$

$$\mathbf{D}[\mathbf{u}^{n+1}] \cdot \mathbf{n} = \mathbf{D} \left[\hat{\mathbf{u}} + \frac{\mathbf{f}\Delta t}{\rho} \right] \cdot \mathbf{n} = 0. \quad (5)$$

The velocity field in the particle domain involves only translation and angular velocities. Thus $\hat{\mathbf{u}}$ is split into a rigid body motion ($\mathbf{u}^{RBM} = \mathbf{U} + \mathbf{\Omega} \times \mathbf{r}$) and residual non-rigid motion (\mathbf{u}'). The translational and rotational components of the rigid body motion are obtained by conserving the linear and angular momenta and are given as:

$$M_P \mathbf{U} = \int_{\Gamma_P} \rho \hat{\mathbf{u}} d\mathbf{x}; \quad (6)$$

$$I_P \mathbf{\Omega} = \int_{\Gamma_P} \mathbf{r} \times \rho \hat{\mathbf{u}} d\mathbf{x}, \quad (7)$$

where M_P is the mass of the particle and $I_P = \int_{\Gamma_P} \rho [(\mathbf{r} \cdot \mathbf{r}) \mathbf{I} - \mathbf{r} \otimes \mathbf{r}] d\mathbf{x}$ is the moment of inertia tensor. Knowing \mathbf{U} and $\mathbf{\Omega}$ for each particle, the rigid body motion inside the particle region \mathbf{u}^{RBM} can be calculated.

3. The rigidity constraint force is then simply obtained as $\mathbf{f} = \rho(\mathbf{u}^{RBM} - \hat{\mathbf{u}})/\Delta t$. This sets $\mathbf{u}^{n+1} = \mathbf{u}^{RBM}$ in the particle domain. Note that the rigidity constraint is non-zero only inside the particle domain and zero everywhere else. This constraint is then imposed in a third fractional step.

In practice, the fluid flow near the boundary of the particle (over a length scale on the order of the grid size) is altered by the above procedure owing to the smearing of the particle boundary. The key advantage of the above formulation is that the projection step only involves straightforward integrations in the particle domain.

The above formulation can be easily generalized to particles with *specified motion* (such as the microvalves) by directly setting \mathbf{u}^{RBM} to the specified velocity. In this case, the integrations (equations 6) in the particle domain are not necessary.

The details of the numerical scheme and the implementation can be found in [3, 5]

CONTROLLER DESIGN

Model-based control design requires a reduced order model of the flow dynamics that relates individual channel valve openings with the exit flow velocities for each channel. While direct numerical simulations of the flow field produce the most accurate relationship between these quantities, the computationally intensive nature of these simulations precludes their use in any

real-time physical realization. However, many real-time control methodologies have been developed to control linear, multiple-input, multiple-output (MIMO) systems. The development of a reduced order, linear MIMO model is therefore motivated both by the ability of linear models to adequately represent nonlinear flow dynamics in certain flow regimes as well as the relative success of linear control methodologies in controlling nonlinear systems.

System Identification

As a result, standard system identification techniques [6] are employed to produce a linear model of the flow dynamics which relates channel valve openings (inputs) to channel exit flow velocities (outputs). Specifically, an auto-regressive exogenous (ARX) model [7] of the flow dynamics is developed from direct numerical simulations of the flow regime, in which channel valve openings are varied in a prescribed fashion and the resulting output flow velocities are recorded. While a linear, MIMO ARX model is developed, the relationship between inputs and outputs in the ARX formulation is most easily illustrated for the single-input, single-output case. In this instance a linear difference equation relates the input and output:

$$y(t) = -a_1 y(t-1) - a_2 y(t-2) - \dots - a_{n_a} y(t-n_a) + b_1 u(t-n_k) + b_2 u(t-n_k-1) + \dots + b_{n_b} u(t-n_k-n_b+1) \quad (8)$$

where $y(t)$ is the output, $u(t)$ is the input, n_k is the time delay, n_a is the number of poles, n_b is the number of zeros plus one, and a_i and b_j are constants to be determined via the identification process. The equation for the current output is therefore a function of both values of the output and the input at previous sampling instants. The choice of how many previous input and output values to retain is driven by the model validation procedure, in which the output prediction of the model is compared to the results obtained from direct numerical simulations of the flow for data not utilized in the identification process. In the multi-variable case, the coefficients a_i and b_i become $n_o \times n_o$ and $n_o \times n_i$ matrices, respectively, where n_o and n_i represent the number of model outputs and inputs.

System identification is conducted following the procedure presented in [7]. Uncontrolled simulations are utilized to determine the system settling time, which informs the choice of both the sampling interval and the duration of the identification tests. Identification tests are subsequently conducted via numerical simulations of the flow field, in which channel valve angles are randomly varied to excite all modes of the flow dynamics. Flow velocities at the exit of each channel are recorded and this output data, in conjunction with the recorded variation of the input valve orientations, is processed within the Matlab system identification toolbox to produce multiple linear ARX models of

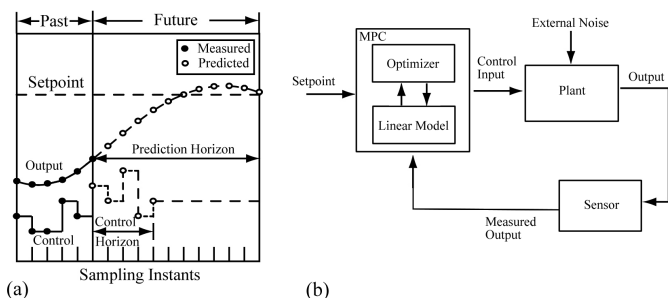


Figure 2: Model predictive control scheme: (a) inputs and outputs and their relation to the control and prediction horizons (b) control system diagram including the model predictive controller.

varying order. Models are validated against numerical simulation data not used in the identification procedure. Channel exit flow velocities are generated by each model from the prescribed variation of the input valves used to produce the validation data set. These velocities are compared to those obtained by direct numerical simulation of the flow field. Model selection is governed by output accuracy, as balanced with model simplicity. The selected linear, MIMO system model is subsequently employed as a substitute for the actual flow dynamics in the model predictive controller design.

Model Predictive Control

A model predictive control (MPC) methodology [8] is employed to equalize flow velocities in a parallel microchannel configuration in the presence of bubble disturbances. Benefits of model predictive control include: real-time optimization of control outputs, direct incorporation of constraints on both manipulated and controlled variables, successful system operation closer to constraints, and robustness to model uncertainty and external disturbances. An overview of the functionality of a model predictive controller is illustrated in Figure 2 and summarized below. For the parallel microchannel configuration studied, the model predictive controller prescribes the valve openings for each channel (control inputs) from knowledge of the desired flow velocity at the exit of each channel (system setpoints) and the actual flow velocities (measured outputs). To determine the valve openings that will result in the measured flow velocities reaching the desired values in the future, the model predictive controller utilizes the linear system model produced by the system identification procedure. Predictions of the exit flow velocities are generated using the model for a user-specified duration into the future (prediction horizon) from a sequence of channel valve openings over a user-specified control horizon. Optimal values for the valve openings are determined, via solution of a quadratic programming problem, over the control horizon such that a cost function

involving the deviation from the desired setpoints is minimized over the prediction horizon. Once the optimal sequence of valve openings is determined, only the first set of openings are provided to the flow solver (plant). At the next sampling instant, the resulting exit flow velocities are measured and sent to the model predictive control scheme. Utilizing this new information regarding the actual flow velocities achieved as a result of the valve openings, as opposed to those predicted by the linear model, the process repeats.

Realization of the model predictive control design is achieved through the Matlab predictive control toolbox. The system model, control horizon, prediction horizon, cost function structure and associated weighting matrices, setpoint values and the measured outputs are input into the MPC toolbox. The quadratic programming problem is solved within the toolbox to produce the channel valve openings utilized by the flow solver. The resulting strategy is computationally lightweight, enabling future physical implementation with small microcontrollers.

VALIDATION CASES

The numerical formulation together with the control algorithm are first used to perform some basic validation and verification studies. The numerical test cases were chosen to validate the basic incompressible flow algorithm applied to high-aspect ratio channel flows, flow developed by objects undergoing specified motion to test the capability of the solver to handle moving microvalves, motion of freely moving particles and bubbles, and finally testing of the coupled CFD-control algorithm. After these extensive validation studies, the coupled solver is applied to mitigate flow maldistribution in parallel microchannels.

Microchannel case

This test case involves full three-dimensional simulation of laminar flow in a microchannel studied experimentally as well as numerically by Qu et al. [9]. Flow through the plenum and a single microchannel at different Reynolds numbers ($Re_{ch} = 196$ and $Re_{ch} = 1895$ are presented here) were simulated. Velocity profiles are used to compare with the experimental and numerical results of Qu et al. [9]. This case is challenging owing to the high aspect ratio of the channel (length to height ratio) as well as large ratio of the plenum to channel heights. The channel consists of a rectangular cross-section with length 120 mm , height $694\text{ }\mu\text{m}$ and width of $222\text{ }\mu\text{m}$. A fully developed velocity profile is applied at the inlet of the domain and a convective outflow boundary condition is imposed at the exit. The flow is simulated until a steady state is reached in the channel before collecting the data. Figure 3 shows the comparisons between predicted values and experimental data of Qu et al. [9] indicating good agreement.

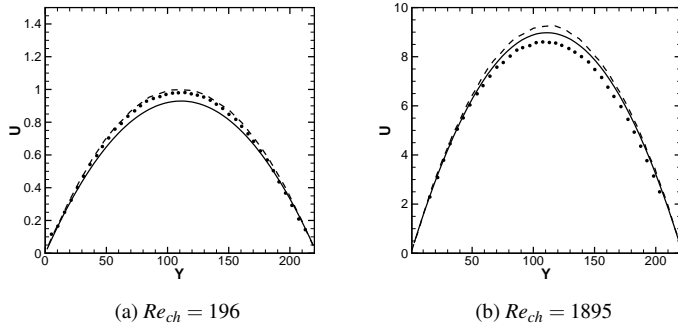


Figure 3: Velocity profile in the fully-developed region. • shows the experimental data, — — — the numerical simulation from [9] and — the present study. The velocity is expressed in $[m/s]$ and the y location in $[\mu m]$.

Oscillating cylinder

Accurate prediction of the flow generated by an impulsively started and oscillating cylinder is crucial to be able to compute the motion of the microvalves used in controlling flow maldistribution in parallel microchannels. Detailed experimental data for the velocity field developed by the cylinder oscillation are available [10]. The computational domain used for this case is $100d \times 100d \times d$ in the x , y , and z directions, where $d = 0.01 m$ is the diameter of the cylinder. The sinusoidal oscillation of the cylinder is specified by:

$$x_p(t) = -A_p \sin \omega t; \quad \omega = 2\pi f; \quad f = 0.2 Hz \quad (9)$$

where x_p is the location of the centroid of the cylinder in the x -direction. The Reynolds number ($Re_d = U_m d / \nu = 100$) and the Keulegan-Carpenter number ($KC = 2\pi A_p / d = 5$) characterize the flow field generated by the oscillating cylinder. The maximum cylinder velocity ($U_m = 0.01 m/s$) is set equal to $10 mm/s$ for this case. The grid resolution in the cylinder region is well refined to allow around 20 grid points to resolve the cylinder. Initially the cylinder is placed at the center of the domain and the flow is at rest. The flow data is collected after 10 cycles of cylinder oscillation. Figure 4 shows the comparison of the axial velocity profile at a fixed location upstream of the centroid of the cylinder with the experimental data to show excellent agreement.

Single sphere rising in an inclined channel

Another example of particle motion has been used to test the scheme: bubble rising in an inclined channel. Like in the simulation the bubble used is a rigid spherical particle. Such a bubble is introduced in an inclined channel the density of

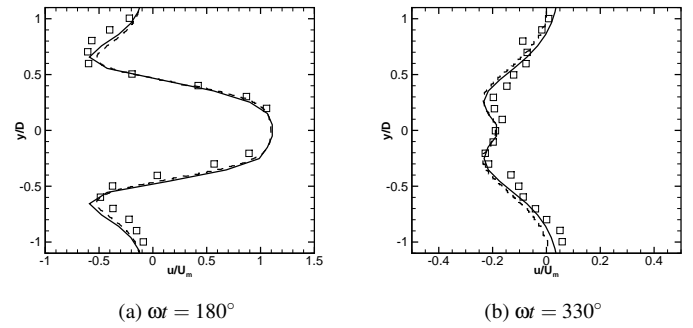


Figure 4: Normalized axial velocity (u/U_m) at three different phase position. The velocity is measured at a fixed x location ($x = -0.6d$) relative to the initial location of the particle center: □ Experimental data from [10]; — present simulation; — — — Numerical results from [11].

the fluid is $\rho_f = 1115 kg/m^3$ and the density of the particle is $\rho_p = 1081 kg/m^3$. The viscosity of the fluid is $\nu = 3.125 mm^2/s$. The Reynolds number $Re_p^{Stokes} = \frac{2aW}{\nu} = 13.6$ based on the Stokes settling velocity W with $a = 2 mm$ is the diameter of the particle.

The domain is a rectangular box of $10 mm$ in the x direction, $80 mm$ in the y direction and $40 mm$ in the z direction. The grid is cartesian and uniform over the domain $40 \times 320 \times 160$ grid points, respectively in the x , y and z directions so that $\Delta = 0.25 \times 10^{-3} m$. The bubble is injected at $x = -1.4 mm$, $y = -1.0 mm$ and $z = 20.0 mm$.

The results of the simulation are compared with experimental and numerical data from [12]. As shown in figure 5 the numerical simulation agrees very well with both experimental and numerical results. The bubble rises with buoyancy and get closer and closer to the right wall of the domain. Ultimately the particle follows the right wall without touching it, keeping a very thin lubrication layer between the particle and the wall.

Equalizing flow rates

Controlled performance was initially validated for the parallel microchannel configuration without a bubble present in any of the channels. In this simulation, a fully developed flow enters a three-channel parallel microchannel configuration. In the absence of any control, the parabolic profile of the inflow and the non-symmetric geometry result in differences in the exit flow velocities in each channel. Figures 6 show the effectiveness of the controlled simulation, in which controlled actuation of the channel valves equalizes the flow rates in all channel branches. The middle valve is closed the most to redirect flow into the outer channels. Ultimately, the exit flow rates equalized for each channel to within 0.16%. The action of the controller can also be seen

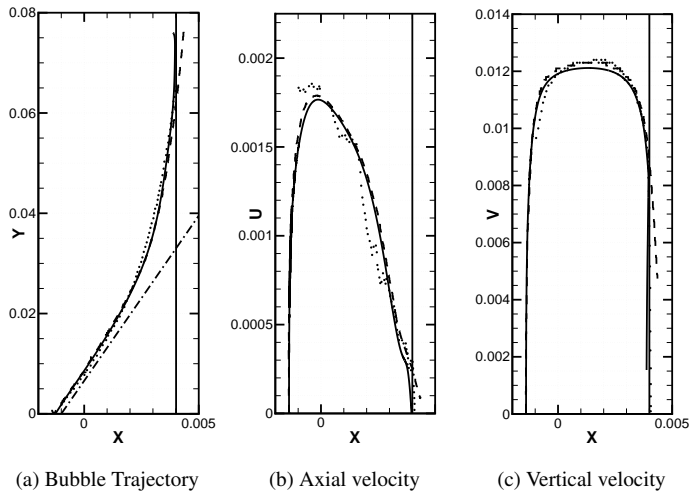


Figure 5: Comparison of experimental \bullet and numerical simulations $---$ [12] with the current simulation $—$. The $---$ line on the trajectory plot shows the initial trajectory due only to the effect of gravity. The particle position is expressed in $[m]$ and the velocities are expressed in $[m/s]$.

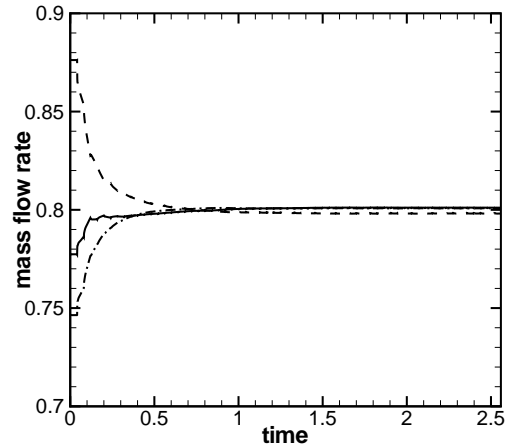


Figure 7: Mass flow rate history. $---$ shows the data for the top channel; $—$ middle channel; $-.-$ bottom channel. Mass flow rate is expressed in $[kg/s]$, time in $[ms]$ and angles in degrees.

PARALLEL MICROCHANNEL SIMULATION

In this section the results for the microchannel simulations are presented. The geometry and the model used for these simulations are presented. Then the effect of a fixed bubble in the geometry are presented. Finally the full simulation with 1 and 2 bubbles are shown.

Geometry and model

As shown earlier the geometry we are looking at consists of 3 microchannels, and 2 plenums for the inlet and outlet. Figure 1 presents the geometry used. The outlet plenum is longer than the inlet in order to avoid effect of the outflow boundary to perturb the flow inside the channels.

The grid is cubic and uniform in the 3 directions so that $\Delta = 0.005 \text{ mm}$. In one channel there are 20 grid-points in the y direction and 160 grid-points in the x direction. Over the entire domain there are 128000 grid-points.

At the inlet boundary of the domain a 2D fully-developed parabolic profile is applied. The maximum velocity at the center of the parabolic profile is defined by $\frac{3}{2}U_p$ where $U_p = 0.6 \text{ m/s}$ so that the global mass flow rate entering the computational domain is $\dot{m} = 2.4 \text{ mg/s}$. The fluid used in the simulation has the same properties as water.

Valves and bubbles

In this simulation, valves have been added in order to control and regulate the flow separately in each channel. The position of the valves is determined by the controller based on the mass-flow rate in each channel. The valves like the bubbles are defined

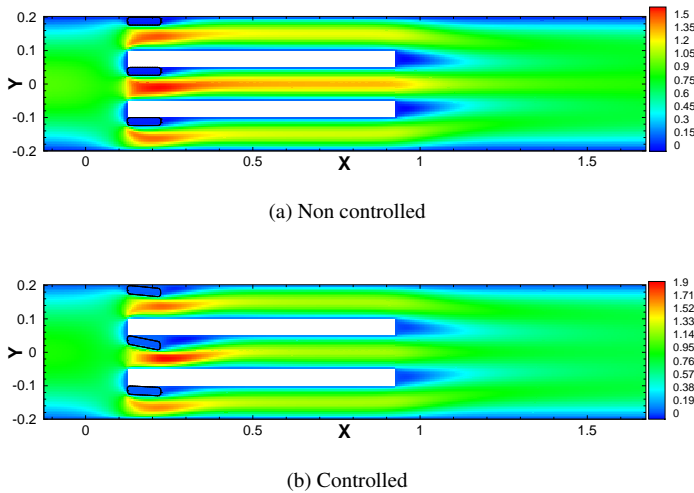


Figure 6: Velocity contour in the 2 parallel microchannel geometry when steady state is achieved. Velocity expressed in $[m/s]$.

by looking at the mass flow rate history (figure 7). The mass flow rate of the three channels converges towards the theoretic value under the action of the controller.

using the fictitious domain approach described earlier.

In order to be consistent experimental observations, bubbles are injected close to the wall. The diameter of the bubble is $6 \times 10^{-2} \text{ mm}$, so that the bubble plugs 60% of the channel height. The bubble is injected close to the entrance of the top channel. Once the bubble is injected it is artificially held fixed at its location.

The simulation conducted here is consistent with the bubble behavior observed in case of bubbly flows ([13]). In this particular regime, the shape of the bubble remains spherical due to low Weber number (which justifies the rigid body approximation) and due to a very small Stokes number, once released, the bubble doesn't perturb the flow.

In a real microchannel with some heat applied at the walls, a bubble would form along a wall and grow, perturbing the flow until the forces (surface tension, viscous forces) are too weak to sustain the hydrodynamic force of the flow ([14]). In order to simulate the effect of the flow on the departure of the bubble, since the growth of the bubble is not taken into account in this simulation, the bubble is held fixed against the wall and the force applied by the flow on the bubble is computed every time step.

Effect of a bubble on the flow

Figure 8 shows the flow without any action of the valves (all channels are fully opened) if a bubble, held fixed, is injected in the top channel. Figure 8a shows the velocity in the domain. The mass flow rate in the unplugged channel has to increase in order to maintain the mass flow rate crossing the domain. Figure 8b shows the pressure contour in the domain. The pressure drops slightly in the same way in both middle and bottom channel but due to the bubble, the pressure drop is larger in the top channel, especially around the bubble itself. Figure 9 presents the consequences of the presence of a bubble on the mass flow rate in each channel. The mass-flow rate in the plugged channel is significantly reduced while it increases slightly in the other channels to respect the continuity through the domain.

Next, we estimate the range of forces acting on the bubble held fixed in the top channel by varying the microvalve configurations. We consider two extreme cases: (a) all microvalves are completely open, and (b) the middle and bottom channel are completely closed by microvalves. In the first case, majority of the flow goes through the middle and bottom branches, whereas in the latter case all flow goes through the top channel. Figure 10 shows the time history of the forces on the bubble in these two extreme configurations. It is found that when the bottom and middle channels are completely closed, the entire inflow goes through the top channel, increasing the hydrodynamic forces on the bubble. The range of the forces applied to the bubble in these extreme configurations vary from $0.013 \mu\text{N}$ to $0.19 \mu\text{N}$.

The magnitude of the force, when the bottom and middle channels are closed, is larger than the forces necessary to hold

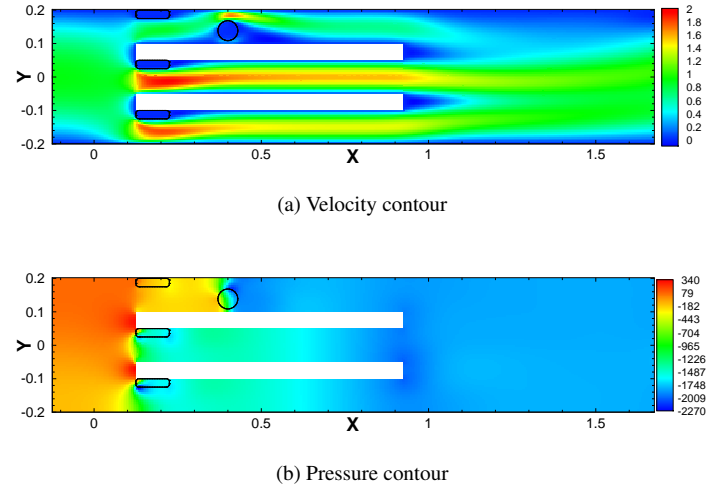


Figure 8: Velocity and pressure contour of flow in the 3 channels geometry with bubble injected and held fixed along a wall. The lengths are expressed in $[mm]$, the velocity in $[m/s]$ and the pressure in $[Pa]$.

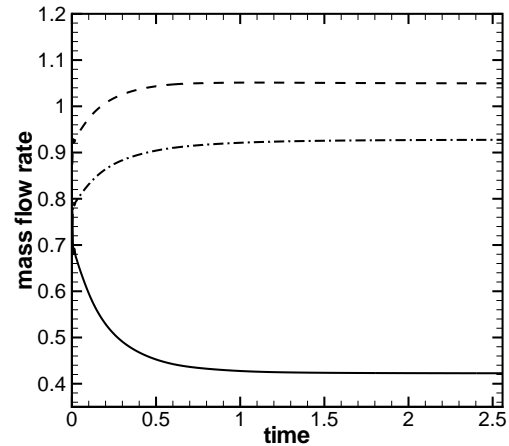


Figure 9: Mass flow rate history measured at the end of each channel. — shows the data for the top channel; --- middle channel; -.- bottom channel. The mass flow rates are expressed in $[mg/s]$ and the time in $[ms]$.

the bubble fixed, estimated based on the surface tension forces, and thus the bubble can be removed by increasing mass flow rate in the top channel. Without any actuation (i.e. all valves are completely open), the hydrodynamic force on the bubble is insufficient to overcome the estimated surface tension forces, and thus the bubble will remain fixed inside the top channel. The goal of the controller then is to first detect flow maldistribution

and then activate microvalves such that the flow rate inside the top channel is increased sufficiently to remove the bubble. This is achieved by slowly activating the microvalves in the middle and the bottom channel.

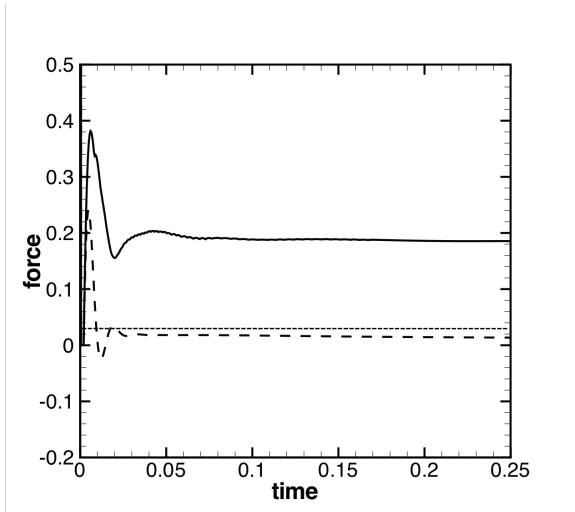


Figure 10: Temporal evolution of the total force acting on the bubble: — — — all channels are open, — the middle and bottom channel are completely closed. The forces are expressed in $[\mu N]$ and the time in $[ms]$. The horizontal dashed line represents the threshold inertial force necessary to set the bubble in motion.

Single bubble simulation

Figure 11 presents the flow history in each channel. At the very beginning of the simulation the mass flow rate is $0.8 mg/s$ for each channel. Then the bubble is injected, the mass flow rate drops in the top channel and increases in the 2 other channels as expected. The controller detects the change in the mass flow rate and starts closing the center and bottom channels until enough flow is forced to go through the plugged channel in order to release the bubble. As mentioned earlier, once released the bubble flows at the same speed as the flow, therefore the controller just has to equalize the flow again in order to get back to the nominal equalized regime.

The bubble has a fairly straight trajectory as long as it remains inside the channel. As soon as it exits the channel the bubble slowly goes down towards the center line of the domain ($Y = 0$).

For the controller aspects, figure 12 presents the control action, in terms of microvalve angles, as prescribed by the model predictive controller. As soon as the bubble is injected the controller starts closing the valves in the middle and bottom channel

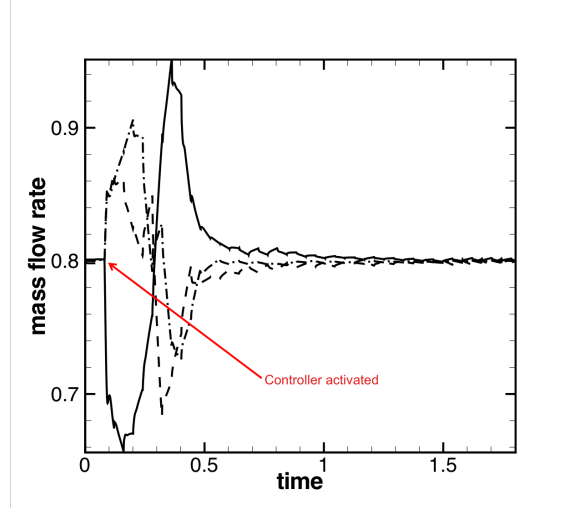


Figure 11: Mass flow history in each channel at $t = 0.04 ms$. — shows the data for the top channel; — — — middle channel; -.- bottom channel. The time is expressed in $[ms]$ and the mass flow rate in $[mg/s]$.

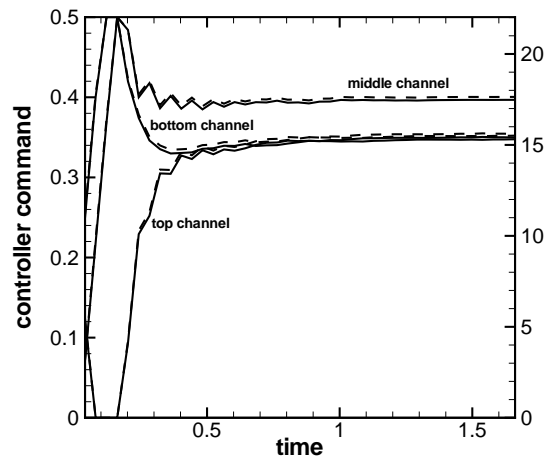


Figure 12: Controller output history correlated with angle applied to each valve.— shows the controller orders; — — — shows the angle applied to the valves. Time is expressed in $[ms]$, angles are expressed in degrees.

and fully opens the top channel. Once the bubble is released and doesn't present any resistance to the flow anymore, the controller starts equalizing the flow to resume a nominal flow inside each channel. A final value of the angle is achieved corresponding to a new equalized steady state.

Multiple bubbles simulation

The full simulation has been achieved using a single bubble in one channel. A simulation using two bubbles is now conducted. In this situation two bubbles are injected in two separate channels. This case becomes more challenging since the controller has now to take care of two bubbles. This simulation has been run with the same controller as in the previous case. The conditions remain the same. The two bubbles are injected at the same time in a stationary steady state achieved by the controller. The force acting on each particle is monitored and each particle is released separately. The controller, by trying to achieve the same mass flow rate in each channel, increases the force acting on each particle until the particles are released.

Figures 13 present velocity contour at different stages of the simulation. They all show the effects of the valves and/or the bubbles on the flow. Figure 13a shows the velocity contour in the domain after the bubbles have been injected. The presence of the bubbles increases the flow rate in the central channel and highest speed regions are found above each bubble. This is confirmed by figure 14 which shows that the lowest pressure region is above the bubbles. The range of velocity is already pretty wide, it can be noticed that the lowest velocity is negative and is located in the wake of the valves where a recirculation zone may occur. Once the controller is turned on it detects the drop in the mass flow rate caused by the introduction of the 2 bubbles. Figure 15 shows the history of the mass flow rate in the 3 channels. It starts with a steady equalized mass flow rate until the bubbles are injected. The mass flow rate in the center channel is increased while the mass flow rate in the two other channels drops. The distribution of the mass flow rate is almost perfectly symmetric over the domain despite the fact that the 2 bubbles are not inserted at the same x location. The controller starts acting on the valves and starts regulating the mass flow rate in each channel. As shown in figure 13b the controller starts closing the center valve since it has detected a drop in the the mass flow rate in both the top and bottom channels. The valves of the plug channels are fully opened.

Figure 15 shows a sudden jump in the flow rate of the bottom channel when the bubble is released, at the same time the flow rate drops in the top channel (still plugged) since the bottom channel is fully opened and offers a wide open path to the flow. Since the bubble in the bottom channel is introduced further in the channel, the flow is more uniform when it hits the bubble, this makes the bottom to be released sooner than the top one. Figure 13c shows the flow after the bottom bubble has been released. Since it's not producing any perturbation in the bottom channel anymore the controller acts on the center and bottom valves in order to increase the flow through the top channel only. The release of the second bubble is shown on figure 15 when the mass flow rate suddenly increases in that channel. The controller regulates the flow to equalize the flow rate again in each channel.

Figure 16 shows the trajectory of the bubbles throughout the

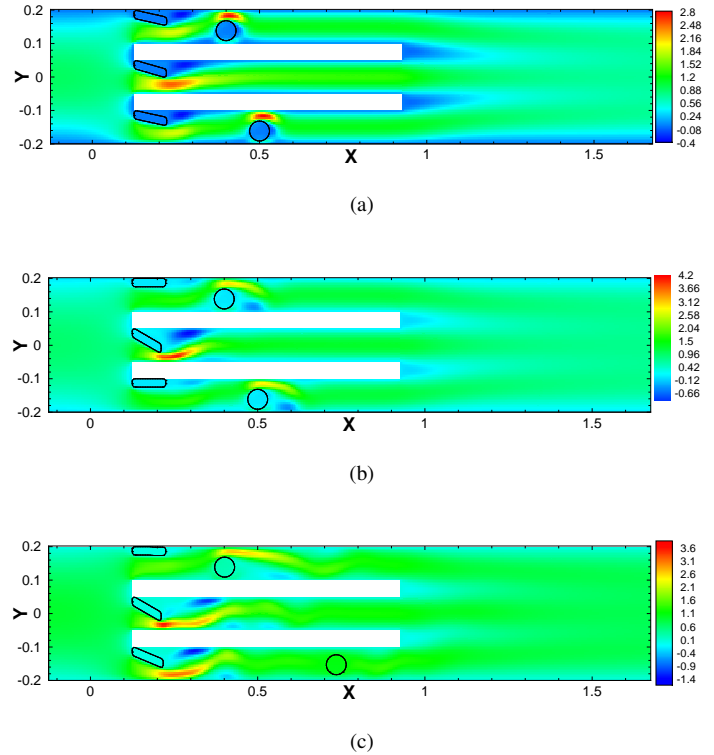


Figure 13: Velocity contour in the domain at different stage of the simulation with 2 bubbles in the domain. The lengths are expressed in $[mm]$ and the velocity is expressed in $[m/s]$.

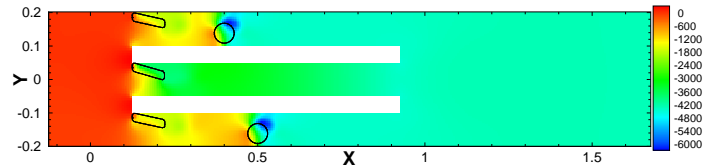


Figure 14: Pressure contour over the domain before the bubbles are released. The lengths are expressed in $[mm]$ and the pressure is expressed in $[Pa]$.

domain. The same observation as in the single bubble case can apply in this situation.

CONCLUSION

In this investigation, direct numerical simulation with fictitious domain representation of immersed objects, such as microvalves and bubbles, was utilized to simulate fluid flow through a parallel microchannel configuration. System identification techniques were able to produce a lower dimensional model that

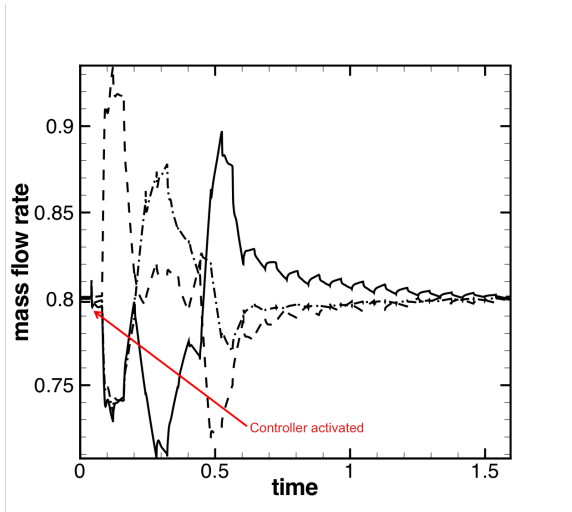


Figure 15: Mass flow rate history measured at the end of each channel. — shows the data for the top channel; --- middle channel; -.- bottom channel. The mass flow rates are expressed in $[kg/s]$ and the time in $[ms]$.

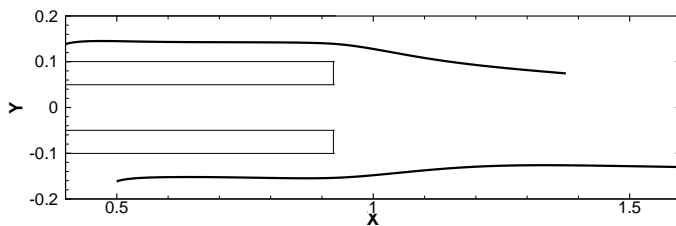


Figure 16: Bubbles trajectory in the geometry. Locations are expressed in $[mm]$.

captured the essential dynamics of the full nonlinear flow, in terms of a relationship between the valve angles and the exit flow rate for each channel.

The resulting linear model was incorporated into a model predictive control scheme to identify flow maldistribution from exit flow velocities and prescribe actuation of channel valves to effectively redistribute the flow. Flow simulations including one and two bubbles in the domain illustrated the effectiveness of the control design, which quickly and efficiently varied channel valves to flush the bubble from the channel and equalize the flow rates in each channel.

ACKNOWLEDGMENT

We would like to acknowledge the US Armys Tactical Energy systems for funding this work through the Oregon Nano

& Micro Institute (ONAMI). All simulations were conducted at the in-house high performance computing cluster. SVA also acknowledges Dr. Ki-Han Kim of the Office of Naval Research for the support provided under the ONR grant number N000140610697. This resulted in successful implementation of the DNS algorithm for freely moving particles.

REFERENCES

- [1] Glowinski, R., Pan, T., Hesla, T., Joseph, D., and Periaux, J., 2001. "A fictitious domain approach to the direct numerical simulation of incompressible viscous flow past moving rigid bodies- application to particulate flow". *Journal of Computational Physics*, **169**(2), pp. 363–426.
- [2] Patankar, N., Singh, P., Joseph, D., Glowinski, R., and Pan, T., 2000. "A new formulation of the distributed Lagrange multiplier/fictitious domain method for particulate flows". *International Journal of Multiphase Flow*, **26**(9), pp. 1509–1524.
- [3] Apte, S. V., Martin, M., and A., P. N., 2008. "A numerical method for fully resolved simulation (frs) of rigid particle-flow interactions in complex flows". *Journal of Computational Physics*, DOI: 10.1016/j.jcp.2008.11.034, **In Press, Corrected Proof**.
- [4] Patankar, N., 2001. "A formulation for fast computations of rigid particulate flows". *Center for Turbulence Research Annual Research Briefs 2001*, pp. 185–196.
- [5] Martin, M., Patton, C., Schmitt, J., and Apte, S. V., 2009. "Direct simulation based model-predictive control of flow maldistribution in parallel microchannels". *Journal of Fluids Engineering*, **Under review**.
- [6] Leung, L., 1999. *System Identification - Theory for the user*. Prentice Hall.
- [7] Zhu, Y., 2001. *Multivariable System Identification for Process Control*. Elsevier Science.
- [8] Camacho, E., and Bordons, C., 2004. *Model Predictive Control*. Springer-Verlag.
- [9] Qu, W., Mudawar, I., Lee, S., and Wereley, S., 2006. "Experimental and computational investigation of flow development and pressure drop in a rectangular micro-channel". *Journal of Electronic Packaging*, **128**, p. 1.
- [10] Dütsch, H., Durst, F., Becker, S., and Lienhart, H., 1998. "Low-reynolds-number flow around an oscillating circular cylinder at low keulegan–carpenter numbers". *Journal of Fluid Mechanics*, **360**, pp. 249–271.
- [11] Kim, D., and Choi, H., 2006. "Immersed boundary method for flow around an arbitrarily moving body". *Journal of Computational Physics*, **212**(2), pp. 662–680.
- [12] Lomholt, S., Stenum, B., and Maxey, M., 2002. "Experimental verification of the force coupling method for particulate flows". *International Journal of Multiphase Flow*, **28**(2), pp. 225–246.

- [13] Cubaud, T., 2004. "Transport of bubbles in square microchannels". *Physics of Fluids*, **16**(12), p. 4575.
- [14] Evelyn N. Wang, Shankar Devasenathipathy, C. H. H. D. W. F. J.-M. K. J. G. S. K. E. G. T. W. K., 2004. "Liquid velocity field measurements in two-phase microchannel convection". In 3rd International symposium on Two-phase Flow Modeling and Experimentation.